Magnesium Map of the Spheroidal-graphite Structure in Ductile Cast Irons

By Haruki Itofuji*

Abstract

In this paper, the author puts forward a new proposal relating to the nucleation and growth mechanism of spheroidal graphite in magnesium-treated cast irons. The Site Theory can not only explain the nucleation and growth mechanism for spheroidal graphite, but can be also applied to the understanding of all other forms of graphite in cast irons. A magnesium map of the microstructure was analysed using EPMA in conjunction with a coloured mapping display system. A Mg halo was found as a segregation around the spheroidal graphite nodules. Although inclusions were observed within some graphite nodules, these also had an Mg halo. These results were considered sufficient to prove the site theory.

Introduction

It has always been the ambition of many workers to understand the nucleation and growth mechanism of spheroidal graphite in molten cast irons, treated with magnesium or magnesium alloy, since spheroidal-graphite iron was invented by H. Morrogh[1] and A. P. Gagnebin.[2] Many researchers have already reported on their theories as to spheroidal graphite nucleation and the growth mechanism. However, no one has yet succeeded in proving their theories in a concrete way. The reason is the failure in these theories to prove, analytically, the role of magnesium from the actual data. Although some workers have attempted to analyse the Mg distribution in the spheroidal-graphite structure, they have not obtained a satisfactory result. For example, W. C. Johnson[3] and S. E. Franklin[4] analysed the distribution of Mg using the Auger technique and the Ion Microbeam Mass Analyser (IMMA) respectively. However, they did not find magnesium in or around the graphite nodules. J. Pirs[5] and H. Fidos[6] also analysed the distribution of Mg using, respectively, X-ray spectrometry and IMMA. In this case, they discovered Mg within the nuclei in some graphite nodules, but an absence of Mg in any other region. Furthermore, since an object is not always to be found in a graphite nodule during a general observation, the investigators' results are not sufficient to explain the spheroidal graphite nucleation and growth mechanism. Therefore, it is considered to be of great importance to know the exact distribution of Mg in s.-g. cast irons when the nucleation and growth mechanism of spheroidal graphite is being discussed and proved.

Table I Chemical composition of mapping analysis specimen

Chemical composition (wt%)									
C	Si	Mn	P	S	Ca	Ce	Mg	Ti	CE
3.53	2.31	0.27	0.037	0.010	0.0027	0.016	0.051	0.013	4.30

CE=C+1/3Si

The site theory, introduced in this paper for the first time, offers a new basis for the understanding of graphite nucleation and growth. Furthermore, the site theory will also be applicable to the nucleation and growth of all types of graphite in cast irons.

In the beginning, the bubble theory proposed by S. Yamamoto[7,8] was adopted as the method of considering the nucleation and growth mechanism of spheroidal graphite. However, after later studies[9,10] carried out on the formation mechanism of spheroidal and compacted/vermicular graphite and other work on graphite precipitation in the solid state[13-20] were checked, a new proposal based on the site theory was advanced and confirmed. This site theory is a developed version of the bubble theory.[7,8,11,12]

The site theory suggests that every graphite form which arises in cast iron is dependent on the site where the graphite precipitated, the substructure depending on the nature of the growth behaviour of the graphite crystal structure at that site. That is to say, the site of graphite precipitation dictates the form of the graphite and its substructure. Furthermore, there is no difference between the liquid and the solid state during graphite precipitation in cast irons if the site has a free surface in both states. This can be ascertained from each graphite substructure.[9,11]

In this study, the distribution of Mg in the microstructure was analysed using EPMA in conjunction with a coloured mapping display system.

1 Nomograph linking density, accelerating voltage and diffusion depth of electron.

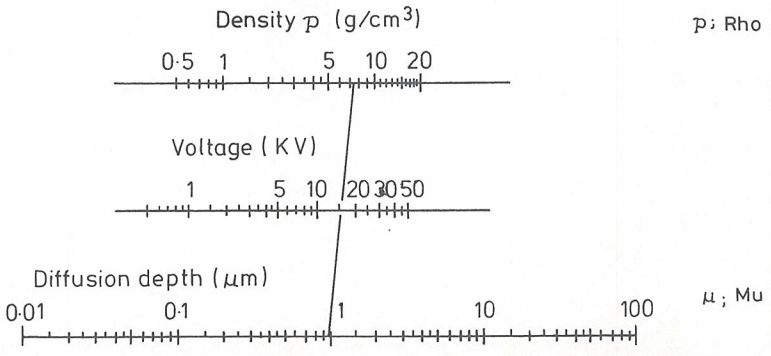

* The author is associated with the Technical Development Group, Ube Steel Company Limited, 1978-19 Okinoyama, Kogushi, Ube City 755, Japan.

Table II Standard specimens for calibration curve on mapping analysis

Element	Standard specimen	
	1st analysis	2nd analysis
C	Graphite	Graphite
Si	Pure Si	Low alloy steel
Mn	Pure Mn	Low alloy steel
P	Steadite (Fe_3P)	Low alloy steel
S	$CuFeF_2$	$CuFeF_2$
Ca	$CaSiO_3$	$CaSiO_3$
Ce	CeF_3	CeF_3
Mg	Pure Mg	MgO
Ti	Pure Ti	Pure Ti
N	Si_3N_4	Si_3N_4
O	SiO_2	MgO

$$Zm = 0.033(V^{1.7} - Vk^{1.7}) \cdot A/\rho Z \quad \text{.....[1]}$$

where:
Zm = Depth of analysed region, μm
V = Accelerating voltage, Kv
Vk = Exciting voltage, Kv
A = Mean atomic mass
Z = Mean atomic number
ρ = Mean density, g/cm^3

$$\delta = d + Zm \quad \text{.....[2]}$$

where:
δ = Total diameter of analysed region, μm
d = Electron beam diameter, μm
Zm = Depth of analysed region, μm

The accelerating voltage and the electron-beam diameter were set at 15 Kv and 2 μm respectively.

2 Microstructure for coloured mapping analysis in this study (2% Nital etch, ×110): (a) photo by optical microscopy; and (b) composite image by SEM.

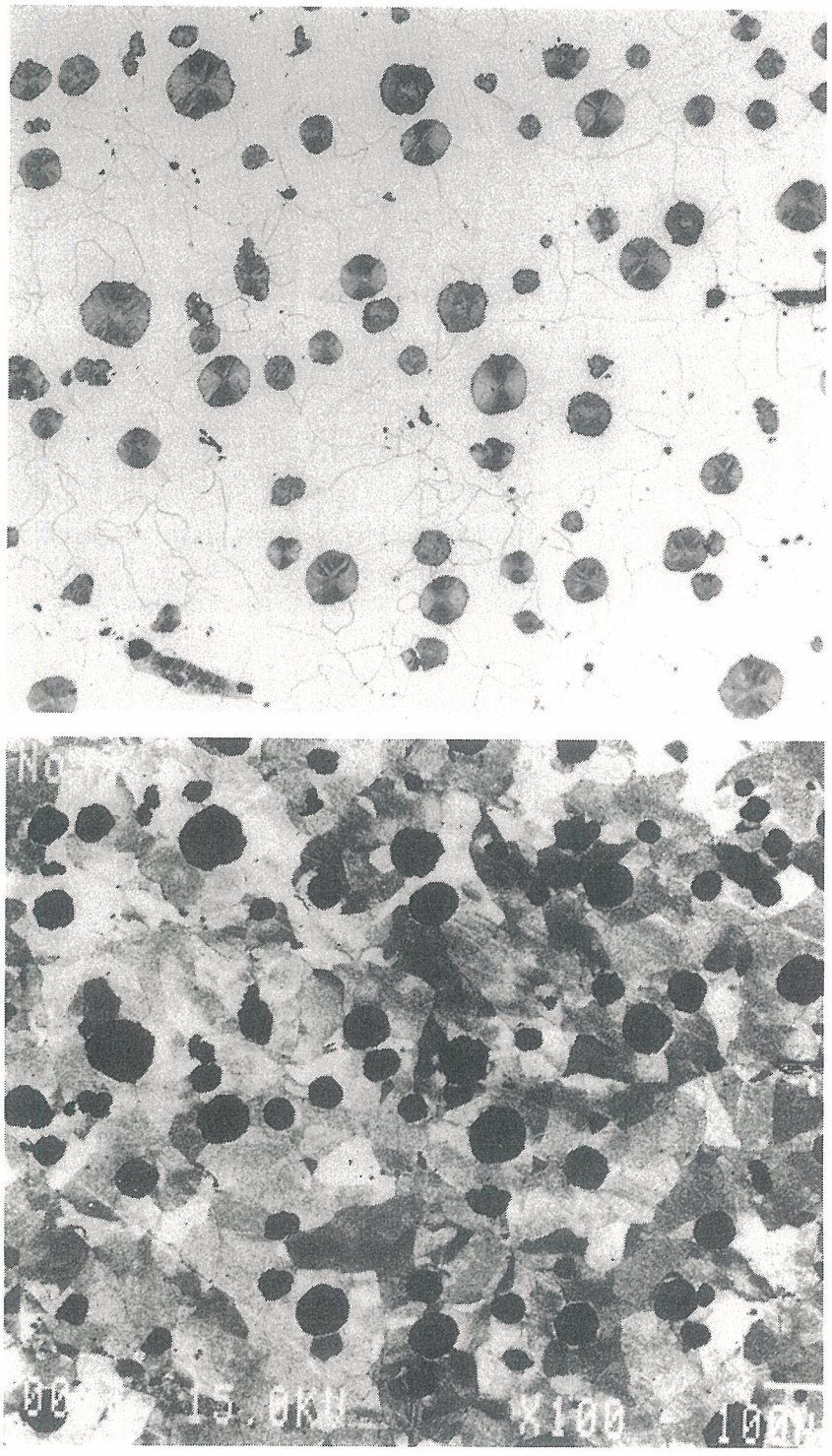

It was considered likely that an Mg halo would surround each graphite nodule, since the Mg gas bubble was the initial site for the precipitation of the spheroidal graphite. Furthermore, Mg, according to the site theory, had almost no solubility in either molten or solid iron. The study described in this paper was therefore carried out to prove and confirm the site theory.

Experimental Procedure

The as-cast specimen 15 by 15 by 10 mm, used for the coloured mapping analysis undertaken in this study, was taken from the upper layer of the 900 by 900 by 150 mm test block. The composition is shown in Table I. The molten metal was prepared in a 10-tonne-capacity low-frequency induction furnace and tapped at 1440°C. The metal was treated in the ladle during tapping with 1.1% FeSi – 5.5% Mg – 1.5% RE and 0.4% Fe-75Si-2Ca-trace Ba, before being poured into a furan-resin-bonded sand mould at 1330°C.

The test specimen was ground, successively, on 240, 400, 600, 800, 1,000, 1,200, and 1,500 grit silicon-carbide paper. After a brief rinse with acetone and drying, the specimen was polished with 2μm diamond paste on a nylon cloth. Lapping oil was added to keep the cloth moist. Next, the test specimen was dipped in acetone to eliminate any oil, rinsed with alcohol, and then dried again. 2% Nital was used as the etchant.

The test specimen was then inserted into an EPMA (a JXA 8600M manufactured by Jeol, Limited) equipped with a coloured mapping display system, the map of Mg and other chemical elements being analysed by the calibration curve method. The standard specimens of each analysed element for the calibration curve are shown in Table II.

Since the thickness of the Mg halo was expected to be quite thin – in the order of Angström units – an accelerating voltage and electron beam diameter were carefully selected in order to obtain better information from the test specimen, because of their effect on the depth and width of the analysed region at the electron bombardment point, according to the following formulae [1] and [2];[21] formula [1] was simplified to provide the nomograph shown in Fig 1.

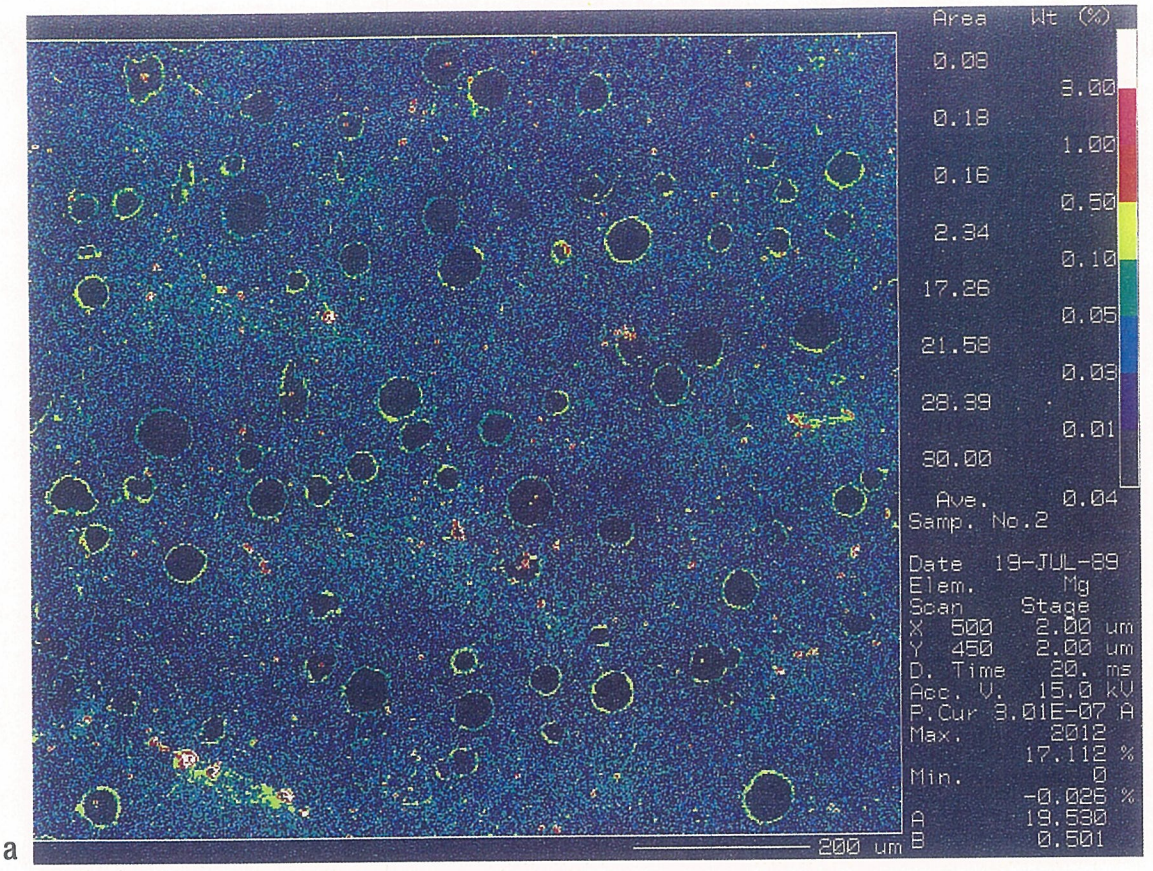

a

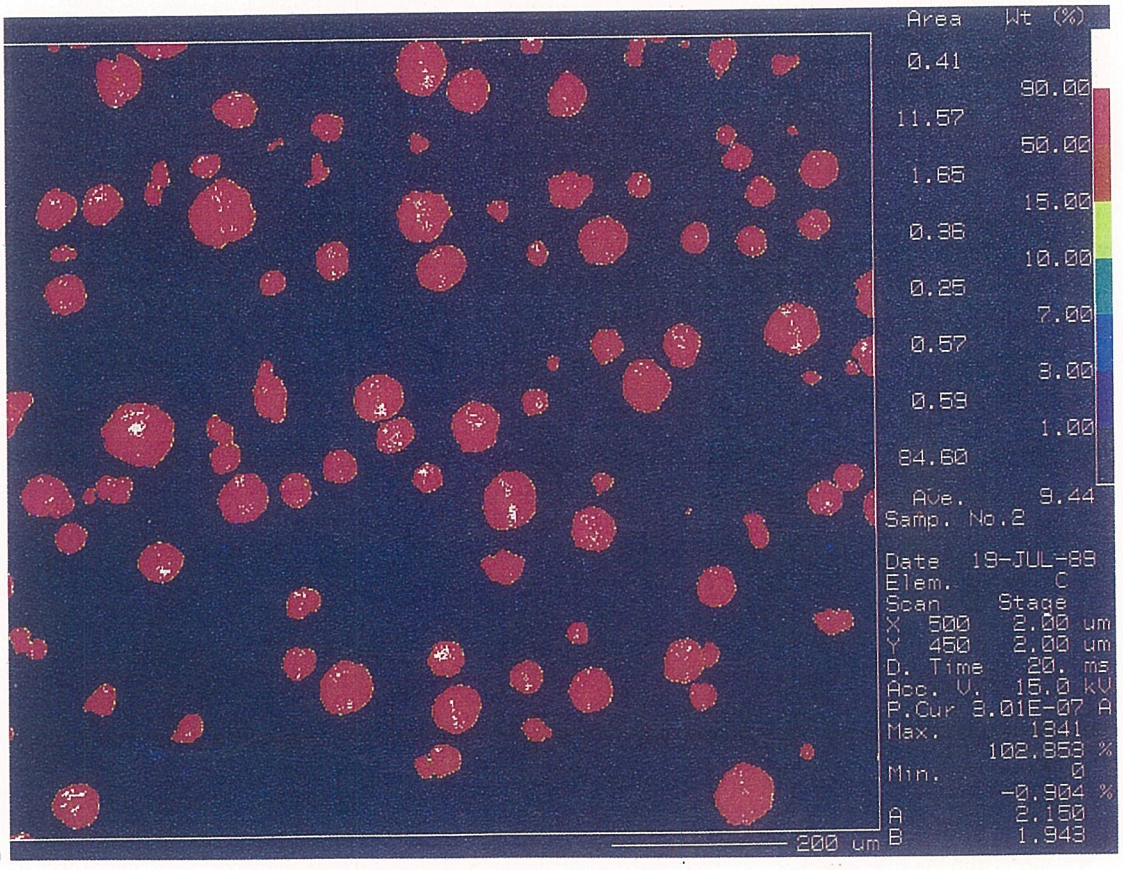

b

3 Result of coloured mapping analysis on microstructure shown in Fig 2. (a) Mg map; (b) C map; (c) Si map; (d) Mn map.

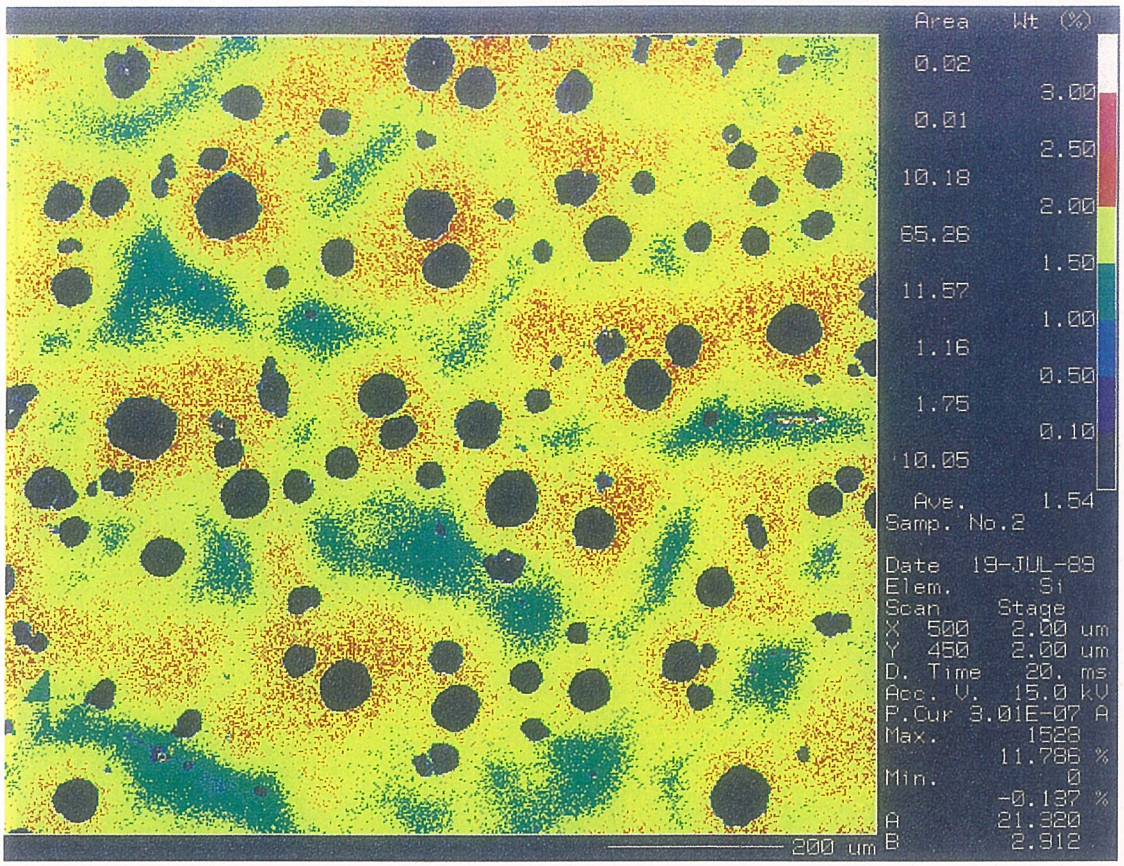
Area Wt (%)
0.02
3.00
0.01
2.50
10.18
2.00
65.26
1.50
11.57
1.00
1.16
0.50
1.75
0.10
10.05
Ave. 1.54
Samp. No.2
Date 19-JUL-89
Elem. Si
Scan Stage
X 500 2.00 um
Y 450 2.00 um
D. Time 20. ms
Acc. V. 15.0 kV
P.Cur 3.01E-07 A
Max. 1528
11.785 %
Min. 0
-0.137 %
A 21.320
B 2.912
200 um

c

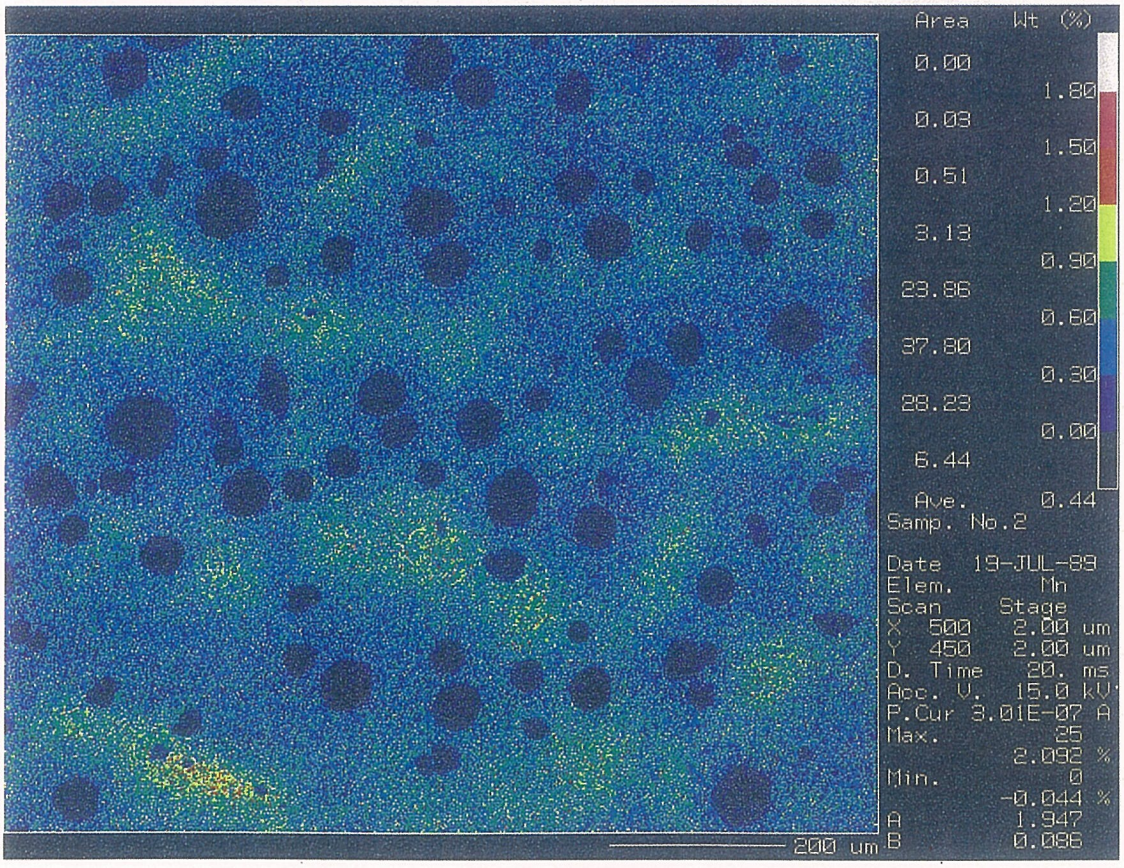
Area Wt (%)
0.00
1.80
0.03
1.50
0.51
1.20
3.13
0.90
23.86
0.60
37.80
0.30
28.23
0.00
6.44
Ave. 0.44
Samp. No.2
Date 19-JUL-89
Elem. Mn
Scan Stage
X 500 2.00 um
Y 450 2.00 um
D. Time 20. ms
Acc. V. 15.0 kV
P.Cur 3.01E-07 A
Max. 25
2.092 %
Min. 0
-0.044 %
A 1.947
B 0.086
200 um

d

3 *(continued)* Result of coloured mapping analysis on microstructure shown in Fig 2. (e) P map; (f) S map; (g) O map; (h) N map.

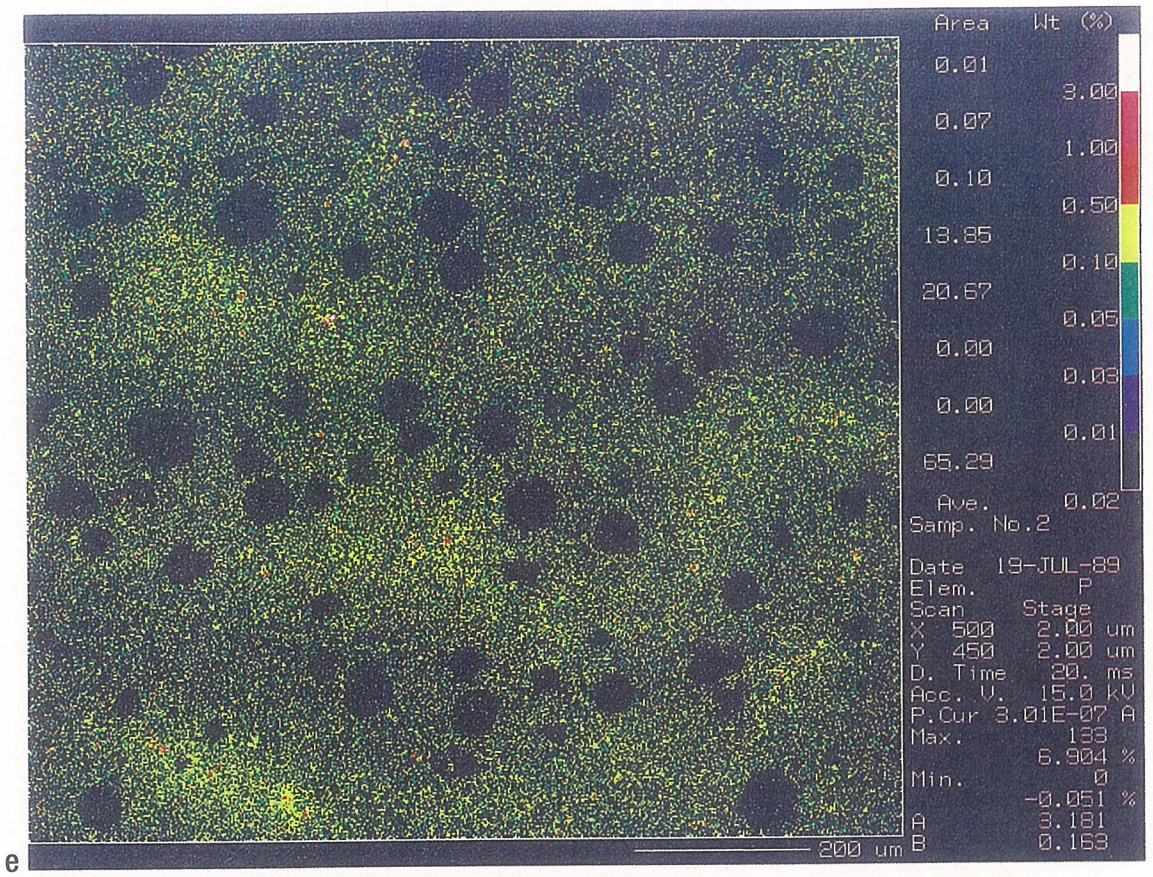

e

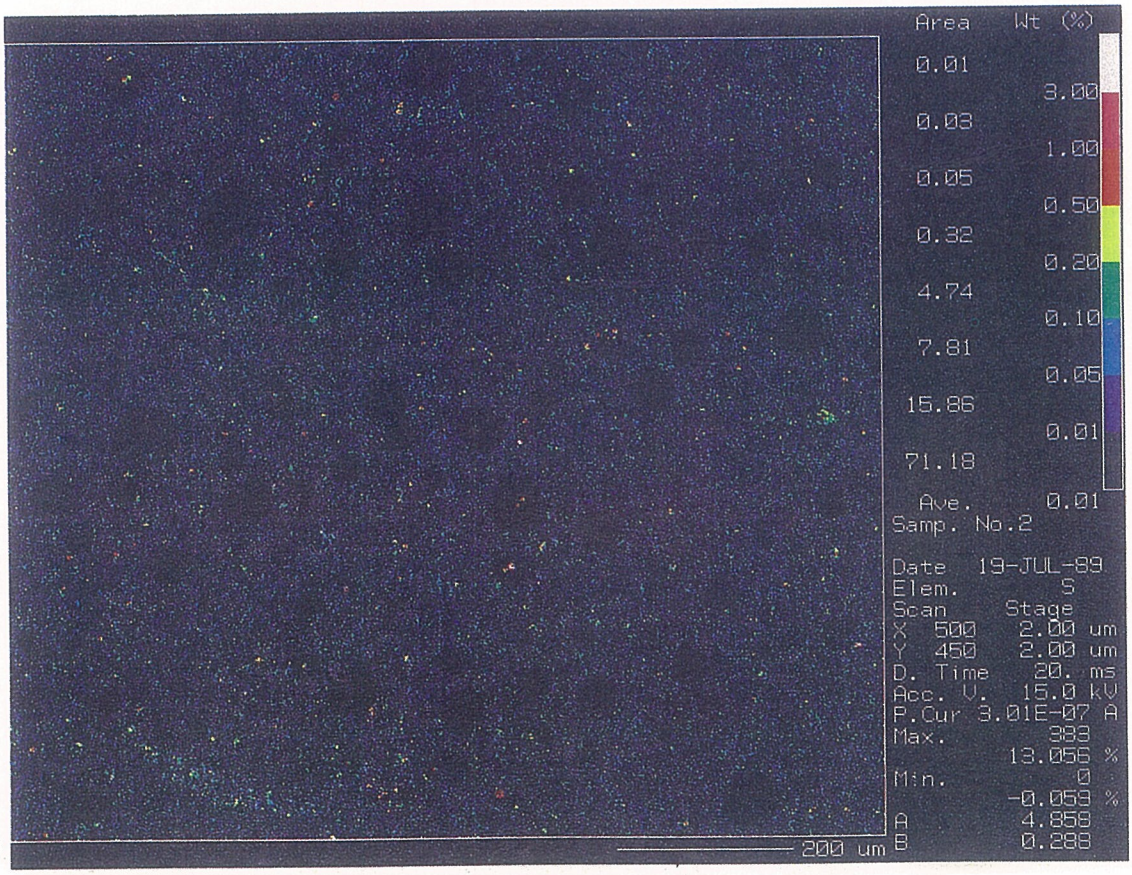

f

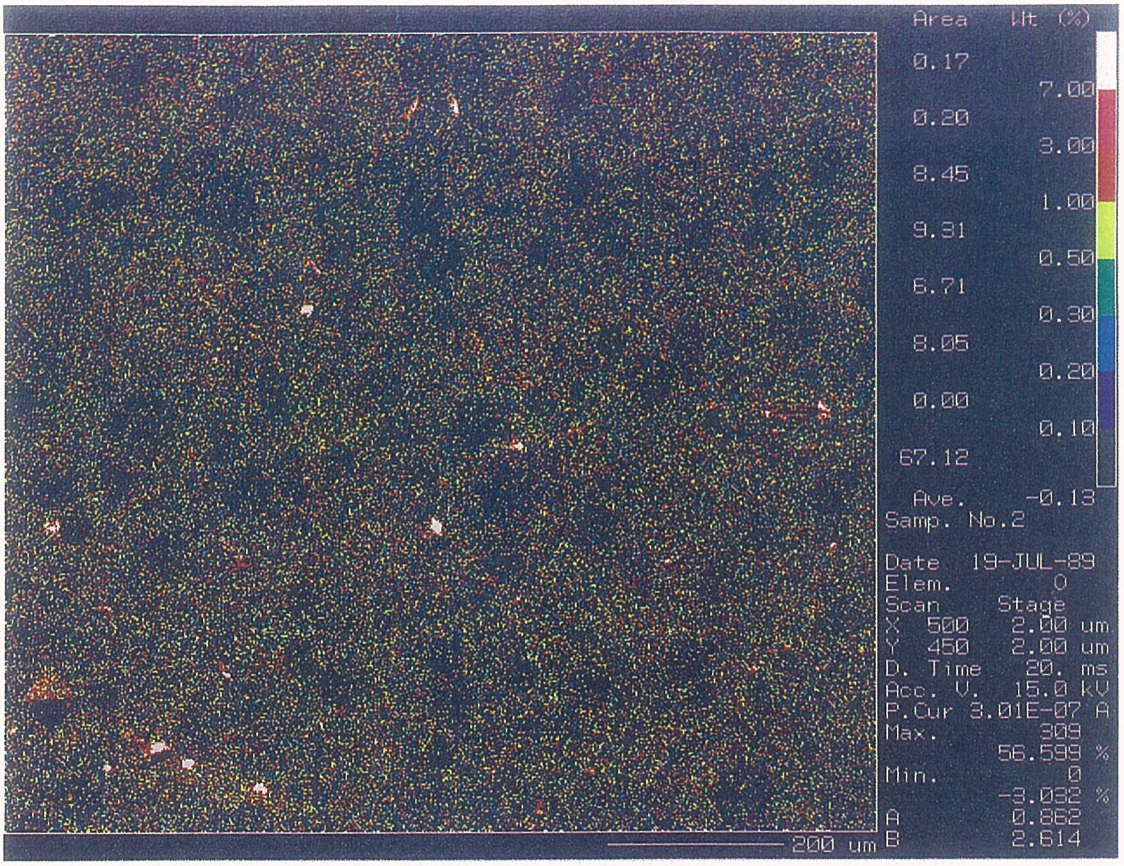
Area Wt (%)
0.17
7.00
0.20
3.00
8.45
1.00
9.31
0.50
6.71
0.30
8.05
0.20
0.00
0.10
67.12
Ave. -0.13
Samp. No.2
Date 19-JUL-89
Elem. O
Scan Stage
X 500 2.00 um
Y 450 2.00 um
D. Time 20. ms
Acc. V. 15.0 kV
P.Cur 3.01E-07 A
Max. 309
56.599 %
Min. 0
-3.032 %
A 0.862
B 2.614
200 um

g

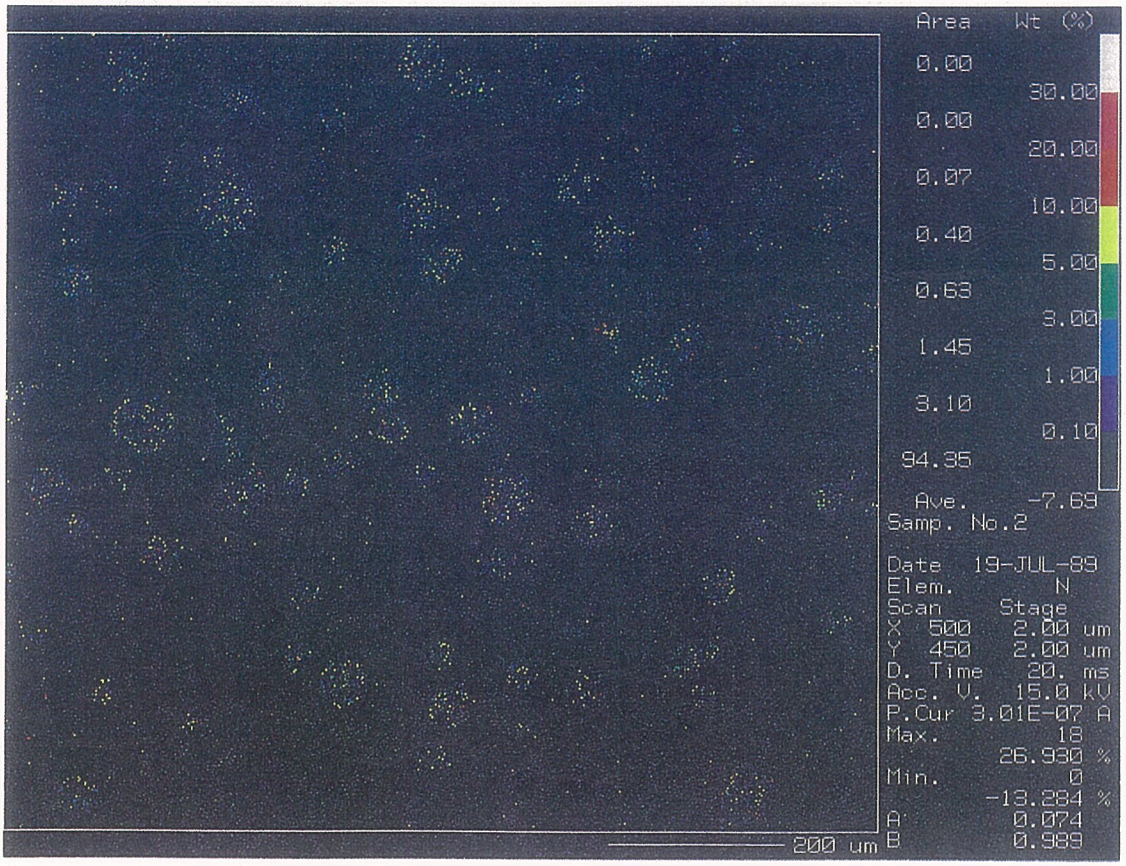
Area Wt (%)
0.00
30.00
0.00
20.00
0.07
10.00
0.40
5.00
0.63
3.00
1.45
1.00
3.10
0.10
94.35
Ave. -7.69
Samp. No.2
Date 19-JUL-89
Elem. N
Scan Stage
X 500 2.00 um
Y 450 2.00 um
D. Time 20. ms
Acc. V. 15.0 kV
P.Cur 3.01E-07 A
Max. 18
26.930 %
Min. 0
-13.284 %
A 0.074
B 0.989
200 um

h

3 *(continued)* Result of coloured mapping anlysis on microstructure shown in Fig 2. (i) Ca map; (j) Ce map; (k) Ti map.

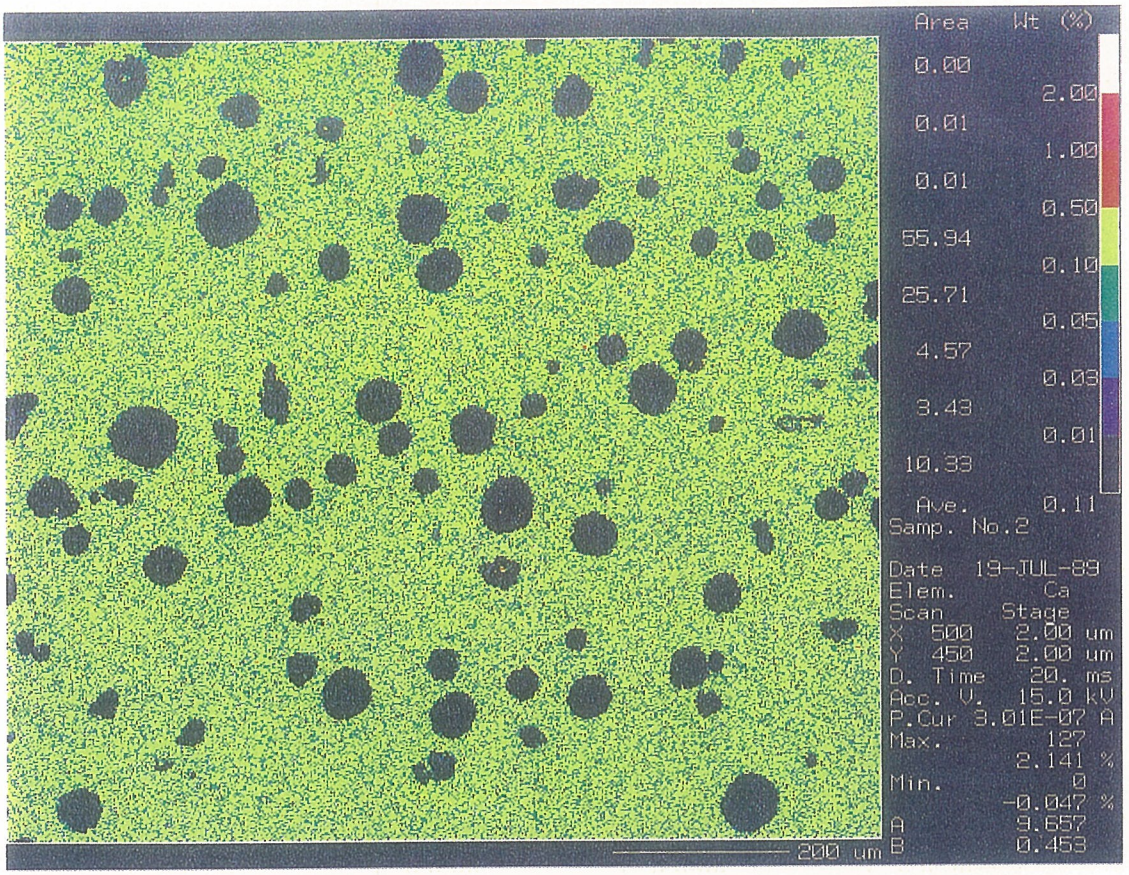

i

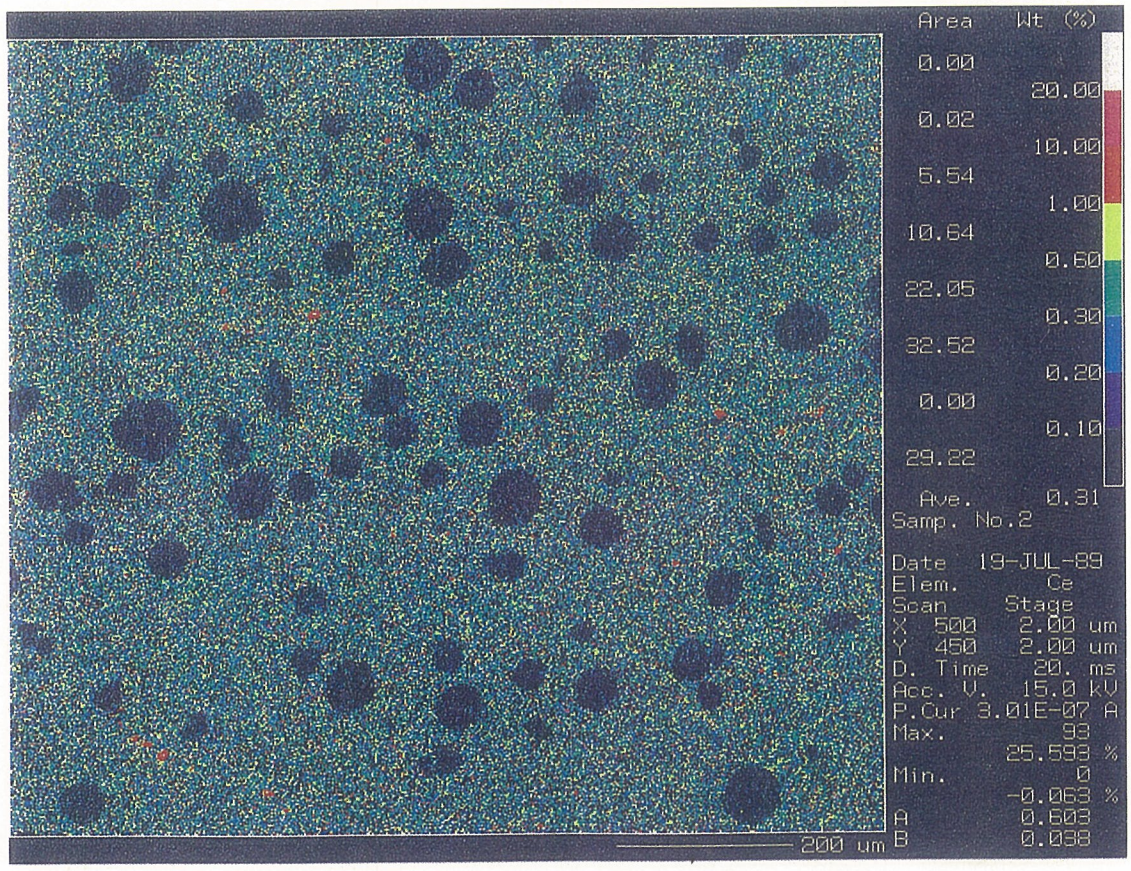

j

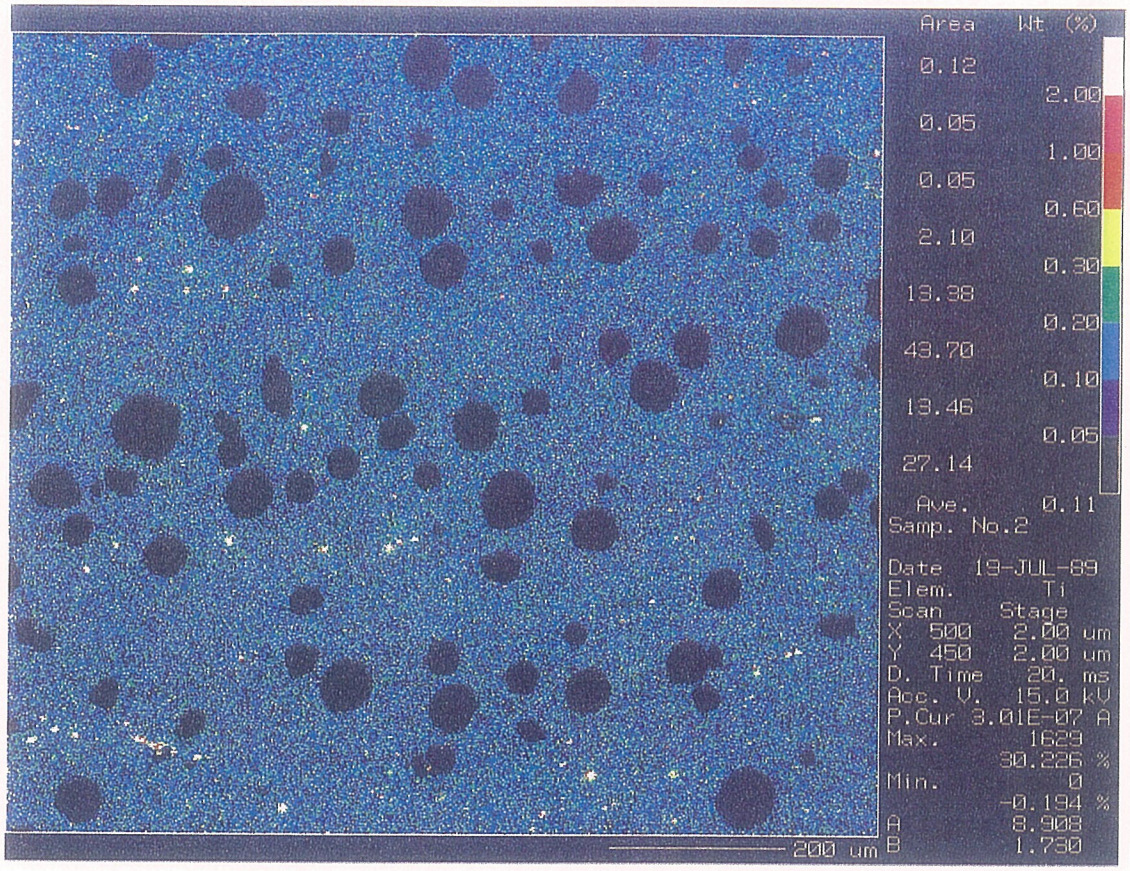

k

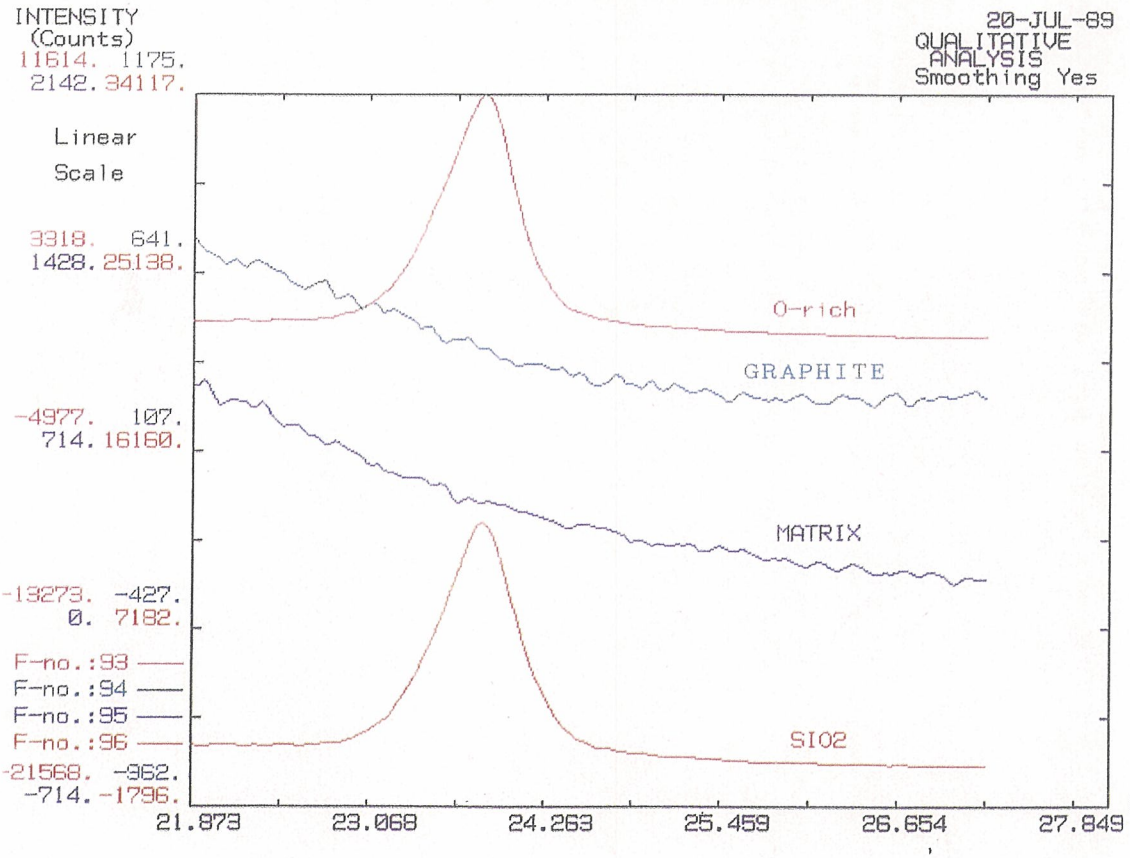

a

4 Element profiles against O and N maps shown in Fig 3 (g) and (h). (a) O profile.

4 *(continued)* Element profiles against O and N maps shown in Fig 3 (g) and (h). (b) N profile.

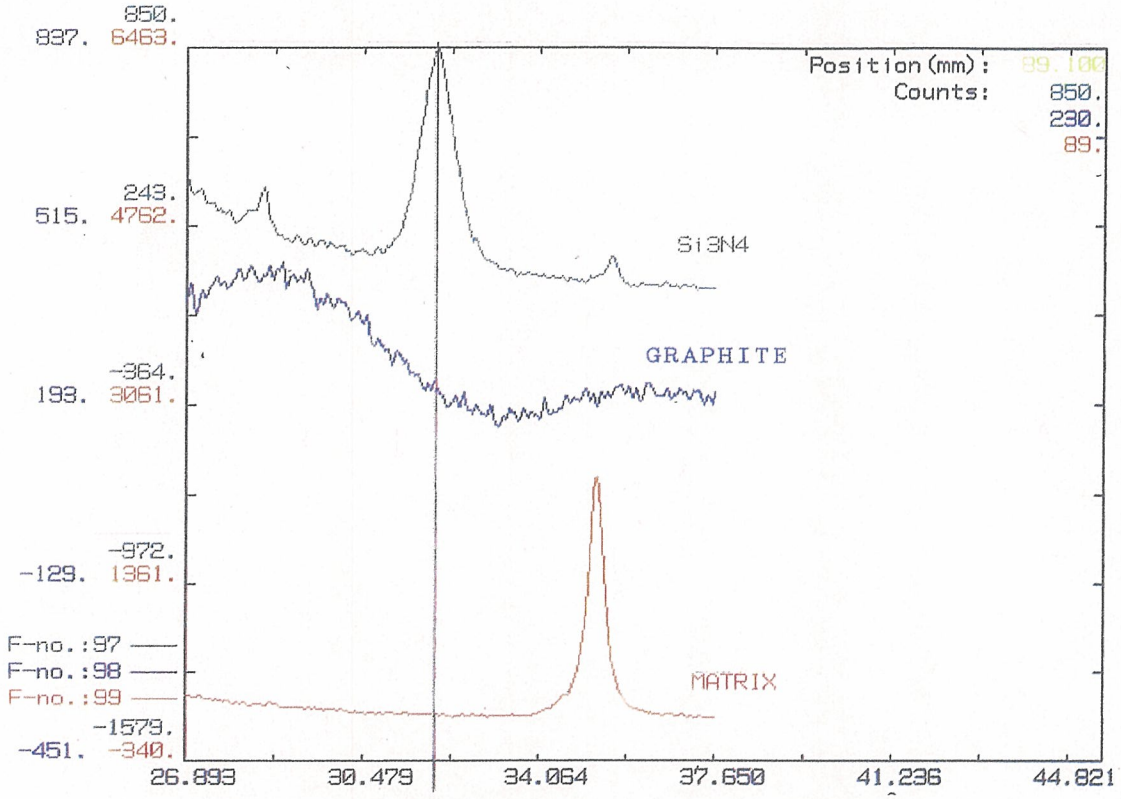

b

5 Central portion of microstructure for re-analysis (2% Nital etch, ×50).

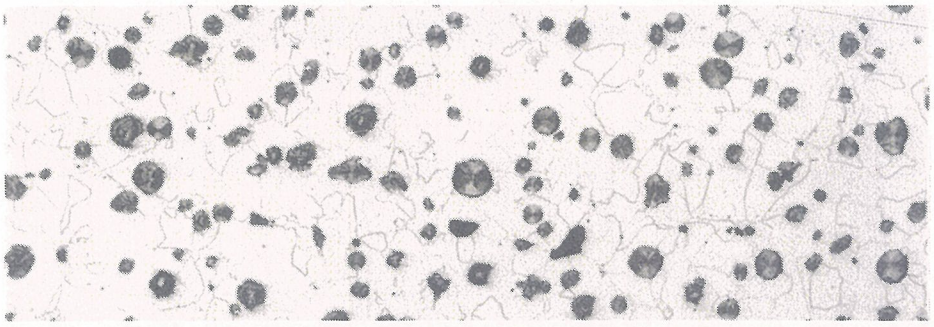

6 Result of re-analysis on O and N maps: (a) O map and (b) N map (opposite).

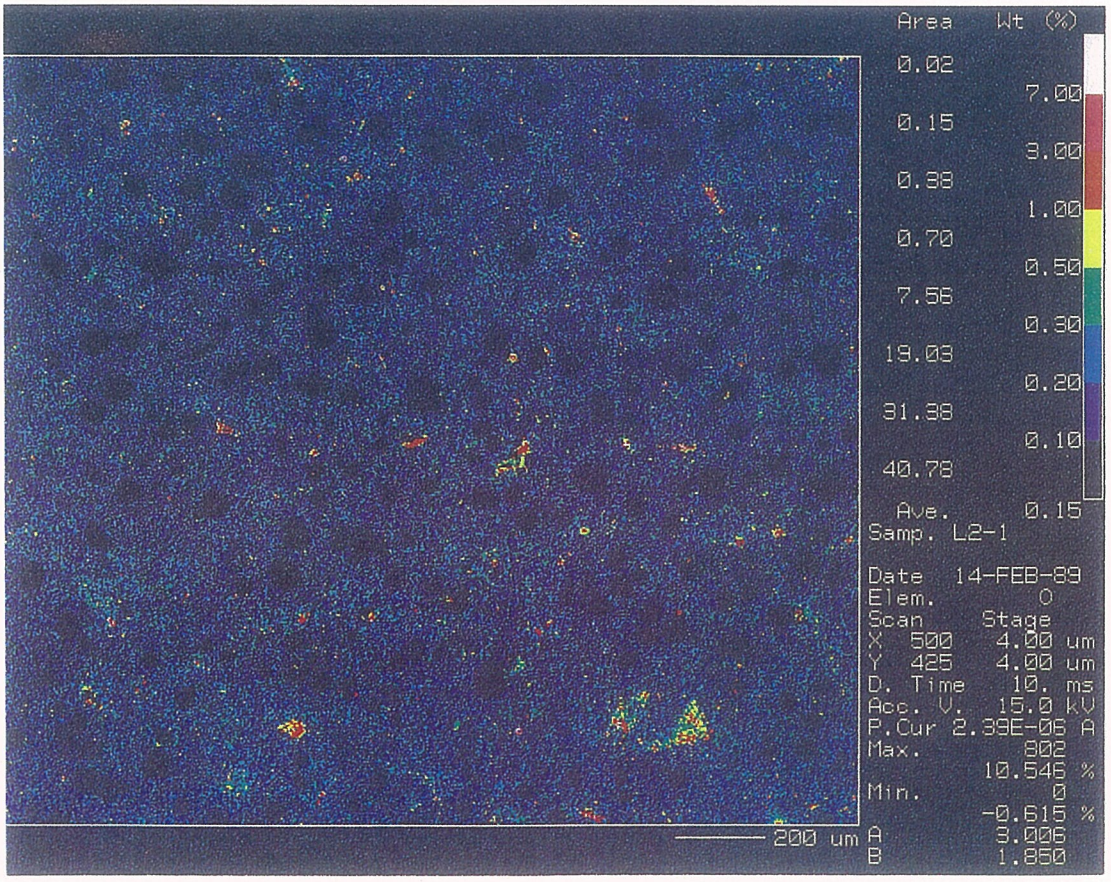

a

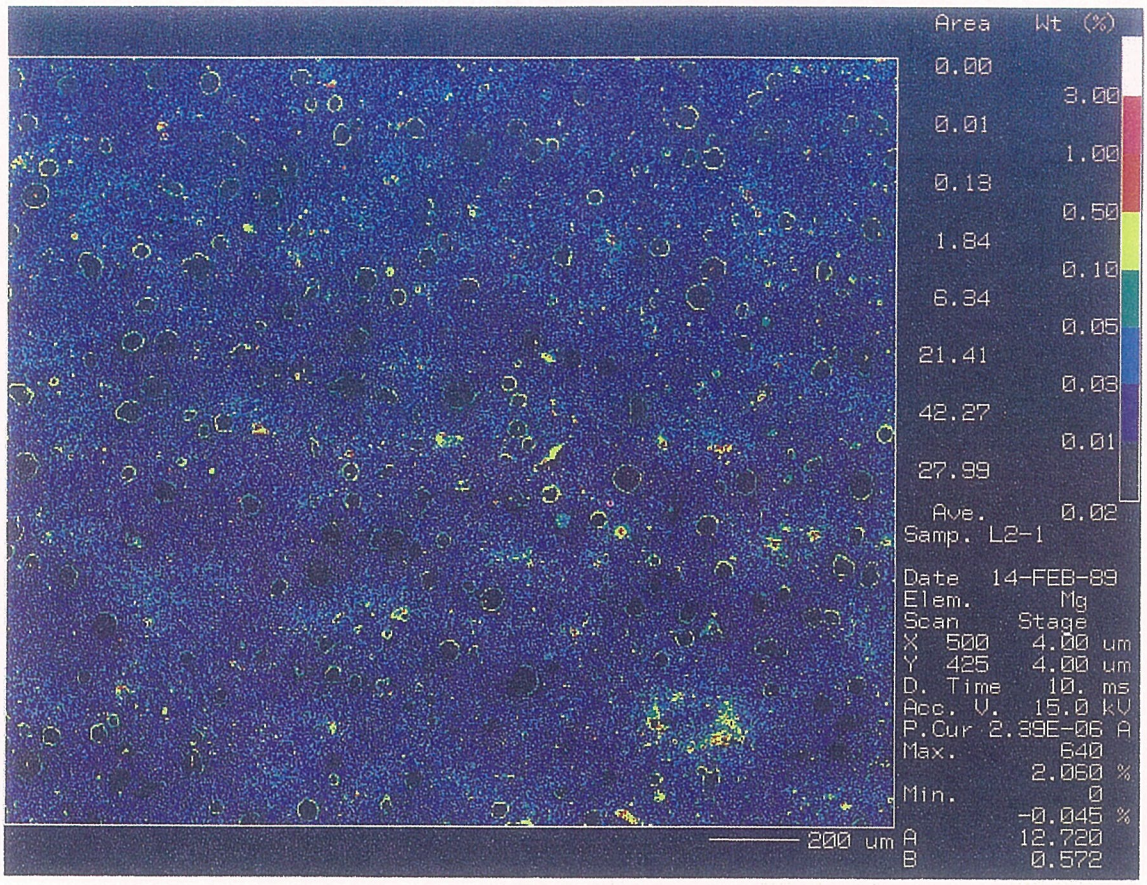

9 (out of sequence) Result of re-analysing on Mg map.

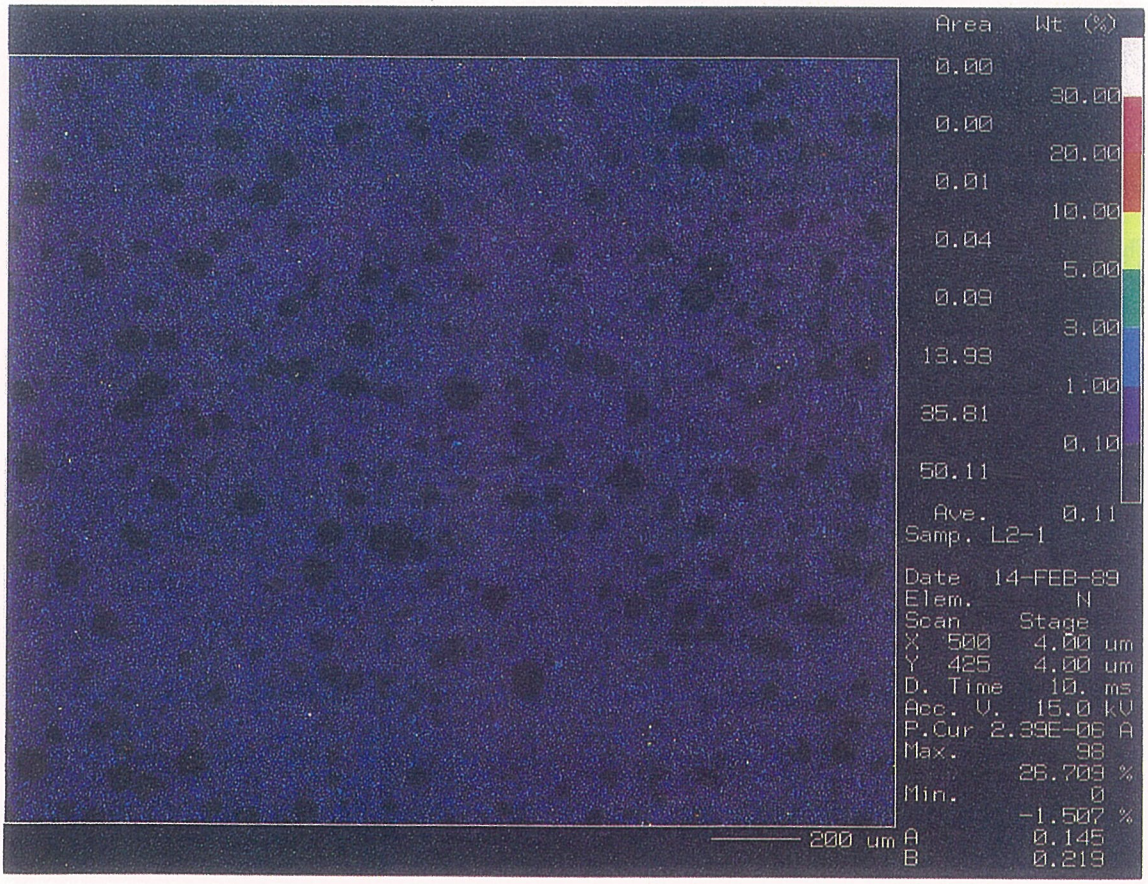

b

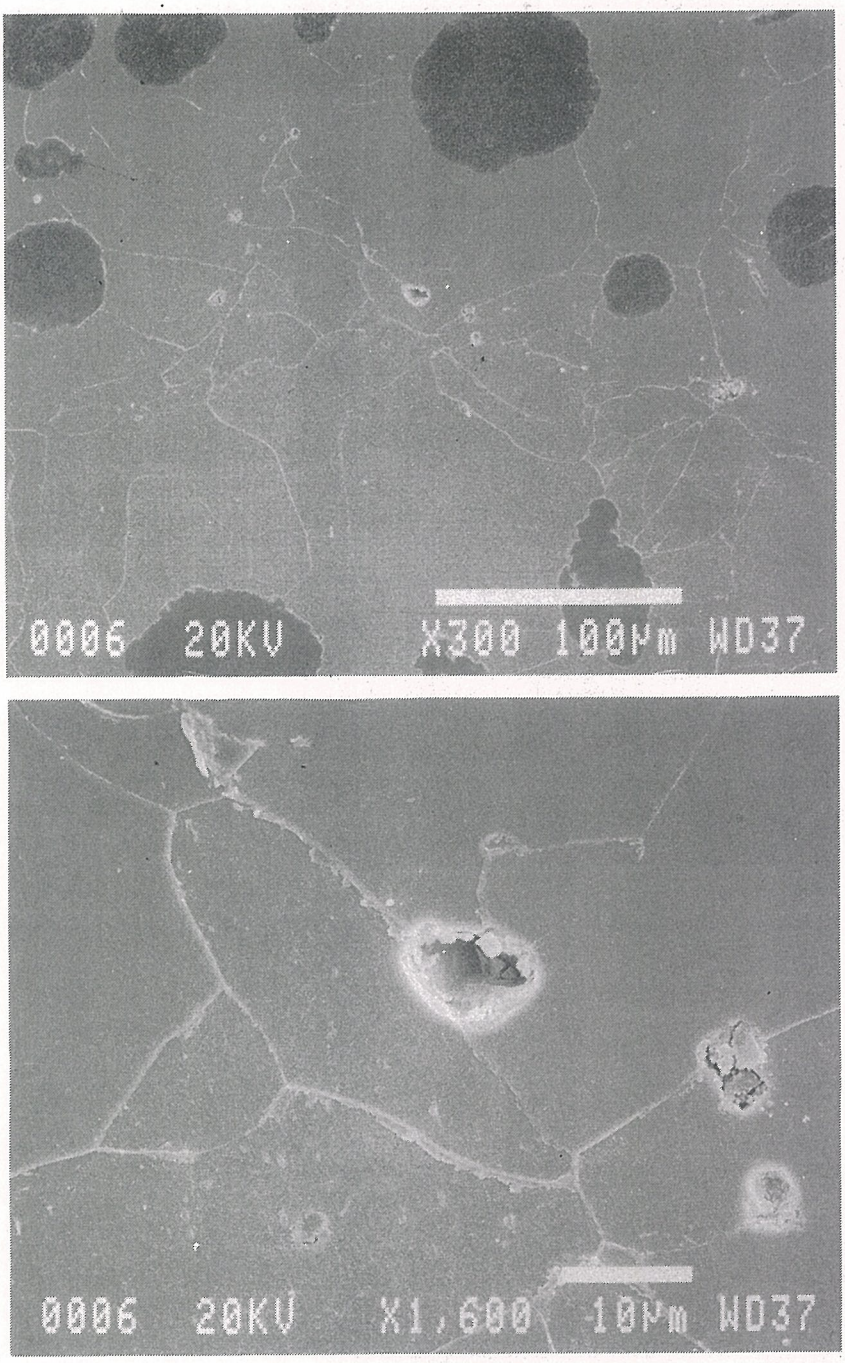

a

b

7 Inclusions amongst old austenite shell with spheroidal-graphite (SEM): (a) inclusions near left upper corner of microstructure shown in Fig 2 and (b) high magnification of SEM (a).

The analysed region for each scanning spot might be, for example, $\phi 3$ µm in area by 1 µm in depth using the above formulae and the nomograph in Fig 1. The analysis was conducted over an area 1.0 by 0.9 mm of the spheroidal-graphite microstructure. It was further divided into 500 elements over the X-axis and 450 elements over the Y-axis. Each element was individually analysed and the precise data yielded by the special X-ray intensity was taken digitally in respect of each. Then, using the computer which forms an integral part of the JXA 8600M unit, the individual data was converted to a weight percentage and the degree of segregation was automatically divided into eight steps, each of a different colour. Since the analytical data could be converted to figures, a small difference in the concentration of the chemical elements amongst those analysed, even down to traces of light elements, could be determined. A spectrum crystal-coating having a layered synthetic microstructure was used in the first analysis.

These extra facilities were not included in the case of a conventional EPMA. The intensity of the special X-ray projected on to the analysed chemical element has been measured by rapid scanning of the electron-beam, as in SEM, whilst the distribution of the chemical elements has been expressed by changes in the tonal density of the white spots. In this case, the instrument has detected the intensity of the special X-ray, over and above a certain level.

The same specimens were re-analysed with a different set of parameters to those used in the first instance. The accelerating voltage and the electron beam diameter were set at 15 Kv and 4 µm respectively. On this occasion the analysed region for each scanning spot might be, typically, $\phi 5$ µm in area by 1 µm in depth. The re-analysis was conducted on an area 2.0 by 1.8 mm in a different part of the microstructure to that originally selected. In this instance, lead stearate acid was used as the spectrum crystal. The standard specimens for the re-analysis procedures are also shown in Table II. The other parameters were set the same as those employed in the first analysis.

Results

The mapping analysis was carried out on the microstructure shown in Fig 2. In this case, the ferrite ratio was more than 95%. The result of the mapping analysis is shown in Fig 3. Since the standard specimen used for the calibration curve was not exclusive to the specimen used in the study, and since the source of the analytical information is only obtained from the surface area, the average value of each of the analysed elements was relatively imprecise. For example, the average percentage of each of the chemical elements did not match the collective analysis set out in Table I. However, the result was sufficiently accurate to provide an indication of the tendency towards segregation.

Segregation in the Matrix Structure

1 *Magnesium*

Magnesium was prominent around the perimeter of every graphite nodule, resembling the halo present in a total solar eclipse. The segregation occurred at the interface between the ferritic matrix structure and the graphite nodule.

It was considered that the halo existed on what was the wall of the old austenite shell. It was observed that there was slight solid solubility of Mg in the matrix structure. The solubility of Mg in the region amongst the old austenite shells associated with spheroidal graphite was greater than that present in the region of the old austenite shells. Mg segregation was observed in the pearlitic region.

2 *Carbon*

Carbon was also very prominent in the graphite nodules at the same position in the microstructure and was present to a small degree in the pearlite region, as is common in such circumstances.

3 *Silicon and Manganese*

As is commonly recorded by many research workers[19,22,23] it was observed that Si segregated negatively and Mn segregated positively. That is to say, Si was in its richest concentration in the region of the old austenite shells associated with the graphite nodules and manganese was in richest concentration amongst the existing austenite shells, especially in the pearlitic region.

4 *Phosphorus*
Phosphorus exhibited a similar phenomena to that of the manganese segregation.

5 *Oxygen and Nitrogen*
A background effect was observed in the case of the O and N map of the graphite nodules. Because of this, both elements within the same microstructure were checked by the wave dispersive method. In this case, the accelerating voltage was also set at 15 Kv, but lead stearate acid was used as the spectrum crystal. As a result, segregation was not observed within the graphite nodule, as shown in Fig 4. The O and N map was again analysed on a different microstructure in the same test specimen using lead stearate acid as the spectrum crystal, since the result was not quite so clear as in the first analysis. The microstructure is shown in Fig 5. O segregation was observed, to a slight degree, in the region amongst the old austenite shells associated with the graphite nodules, especially in the pearlitic region. N segregation was not observed in the matrix structure. The result is shown in Fig 6.

6 *Other Elements*
There was almost no segregation of S, Ti, Ca or Ce in the matrix structure.

Segregation at Inclusions

Most inclusions were observed at the ferrite grain boundaries, especially in the region amongst the old austenite shells associated with the graphite nodules. This area equates to the region which solidifies at a late stage in the eutectic solidification. Examples of the SEM are shown in Fig 7. This view is a highly magnified portion of the microstructure shown in Fig 2, near the left-hand upper corner. Inclusions are observed as black spots in the optical microstructure shown in Fig 2a. These inclusions consist, in the main, of Mg-Ca-Si-P-S-O, Ce-O and TiN systems. Inclusions consisting of the Mg-Ca-Si-S-O system were observed in some graphite nodules. However, those graphite nodules were also surrounded by an Mg halo within the matrix structure. An example is shown in Fig 8. This particular graphite nodule is located at the left-hand upper corner of the microstructure shown in Fig 3a.

Re-Analysis

The map, save for O and N, was also re-analysed in the context of the microstructure shown in Fig 5. In this case, the Mg halo was also observed in the matrix around the graphite. The result is shown in Fig 9. All other chemical elements exhibited the same trends as were present in the first analysis.

Discussion

According to the site theory, graphite nucleation and the process of growth in Mg-treated irons during solidification are illustrated in Fig 10. It is thought that an Mg gas bubble acts as the first site of spheroidal and compacted/vermicular graphite nucleation and growth, at the early stage of solidification. However, a bubble of Mg gas is only the initial site for graphite precipitation in molten cast irons and does not necessarily contribute to the whole growth of spheroidal graphite. After a graphite spheroid is surrounded by an austenite shell, the interface between the graphite spheroid and the austenite shell is the next site for the completion of the growth of the spheroidal graphite. At this point, Mg gas may still exist at the above interface, rather as the earth has an atmosphere, because Mg has almost no solubility in the solid phase. As a result, Mg can remain around a graphite nodule in the form of halo segregation, even after completion of the solidification. In this case, segregation may exist at the wall of the old austenite shell. The above hypothesis was made clear in this study, thus proving the Mg haloes to be a trail of gas bubbles. The poly-crystalline substructure of spheroidal-graphite comes about as the result of the restricted growth in the a-axis direction, of the graphite crystal at these sites.

The initial form of spheroidal and compacted vermicular graphite is the same. However, if there is less magnesium and/or more impurities present than conducive to the formation of spheroidal graphite in molten metal, then compacted vermicular graphite might be formed along the filmy melt channel caused by impurities.

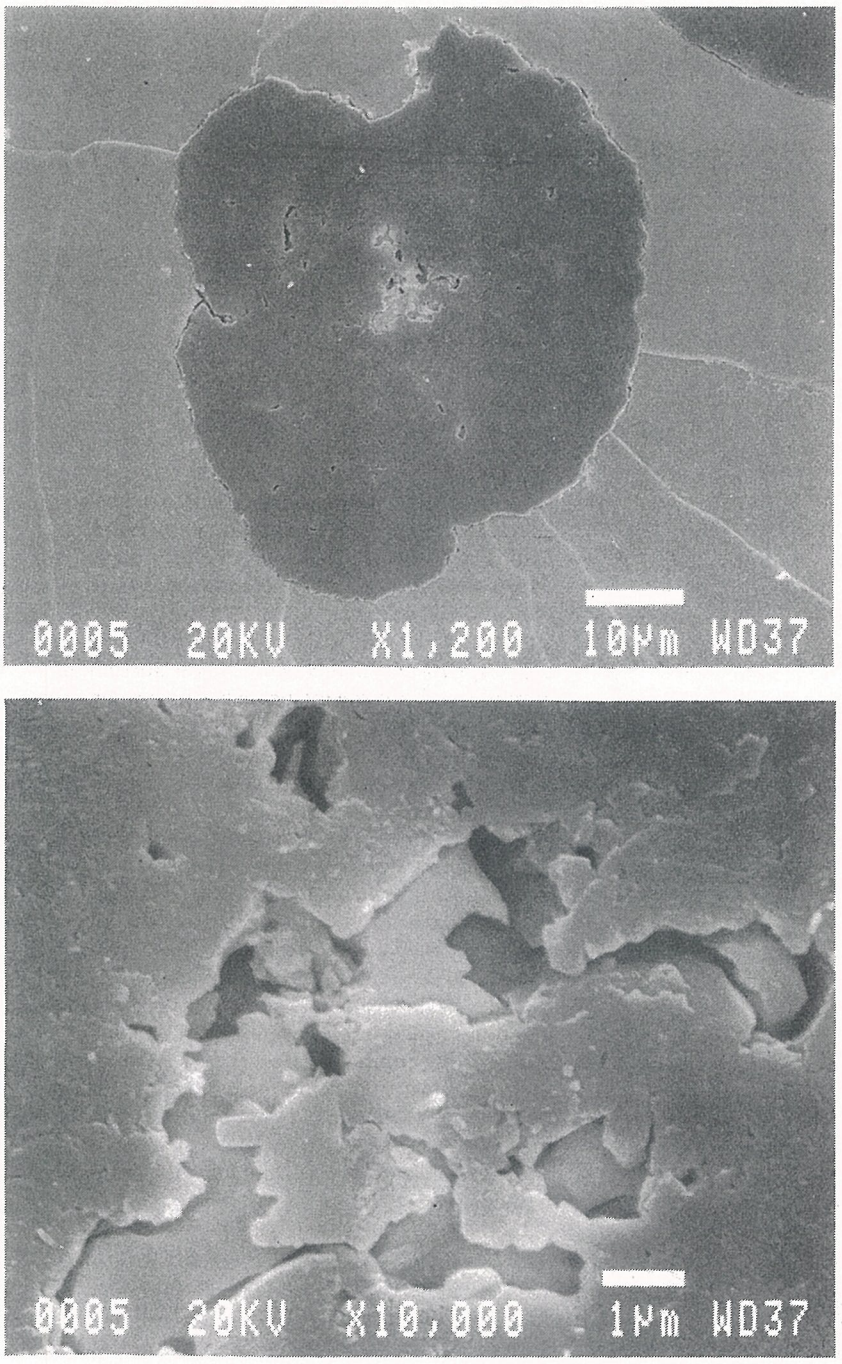

8 Inclusion in spheroidal-graphite (SEM): (a) spheroidal-graphite with inclusion left upper corner of microstructure shown in Fig 3; (b) high magnification of SEM as shown in (a).

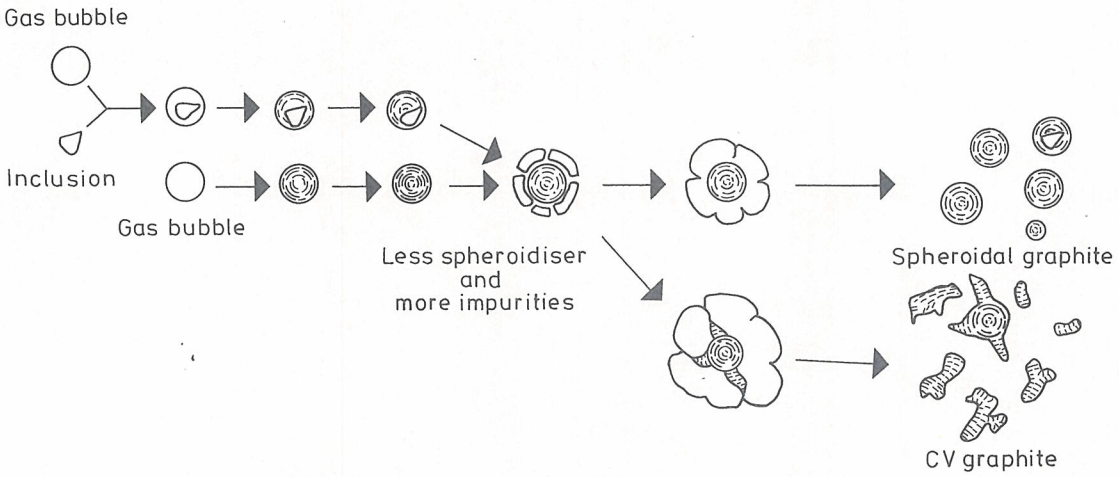

10 Schematic illustration of graphite formation in molten iron treated with spheroidiser.

Some graphite nodules were seen to not only contain inclusions but to be surrounded by a Mg halo. The basic fact is that such inclusions could not dictate the final form of the graphite spheroids even if they acted as the nucleus site for the growth of the graphite. This is the reason why there is no system of bonding between an inclusion and the surrounding graphite, and why the inclusion has no influence on the final form of the graphite sphere nor on the formation of the polycrystalline-like graphite substructure. In point of fact, most inclusions were observed at the ferrite grain boundary amongst the old austenite shells associated with the graphite nodules. This suggests that inclusions do not influence the spheroidal-graphite nucleation during the early stage of solidification, because in the region under observation, the presence of most inclusions equated to the latter stage of solidification. It is thought that such an inclusion becomes trapped on a magnesium gas bubble, graphite subsequently precipitating around the same bubble. As a result, if there were many inclusions present in magnesium-treated iron, then there would be more cases where inclusions were attracted to magnesium-gas bubbles and, as a consequence, entrapped in the graphite nodules.

The distribution of magnesium and its role, as made clear by the site theory, has been determined by use of high resolution EPMA, operated in conjunction with a precise data treatment system. The main purpose has been to prove the presence of a magnesium halo around the graphite nodule. Any gas bubbles introduced by other spheroidisation agents will work in the same way as shown in Fig 10. The stable existence of a gas bubble in molten iron and a spherical void in the austenite shell is important in obtaining a good graphite nodule.

There would appear to be no data available, so far, on the solubility of magnesium in cast iron under atmospheric pressure. In this study, a slight solubility of magnesium has been observed in the ferritic matrix structure. The solubility of magnesium in the region around an old austenite shell associated with a graphite nodule was found to be greater than that present in the region of the old austenite shells. This may be because the vicinity of the old austenite shell is subjected to the eutectic expansion force (maximum pressure $\approx$60 atm)[24]. It is known, furthermore, that the solubility of magnesium obeys Henry's law.[25] Although there is some difference between chemical analysis obtained with a spectrometer and mapping analysis conducted by EPMA, on the total content of magnesium present, the overall tendency can be determined from the result.

Conclusions

As a result of the mapping analysis, the following findings were obtained and made clear:

1 every graphite nodule was surrounded by a magnesium halo;
2 some graphite nodules contained inclusions, although even in these cases, they were also surrounded by an Mg halo;
3 a slight degree of magnesium solubility was observed in the structure of the ferritic matrix;
4 magnesium segregation was present in the pearlitic region;
5 most inclusions appeared in the region of the last stage of eutectic solidification;
6 there was almost no segregation of S, Ce, Ca, Ti, O, and N in the matrix structure, except inclusions, and
7 Si showed negative segregation at the old austenite shells associated with spheroidal graphite, although, on the contrary, Mn and P showed positive microsegregation amonst the old austenite shells, especially in the pearlitic region.

Acknowledgment

The author would like to acknowledge the helpful comments of Dr. Paul Hideo Shingu of Kyoto University in the preparation of this presentation.

References

1 J. H. Morrogh and W. J. Williams, "Graphite Formation in Cast Iron and in Nickel-Carbon and Cobalt-Carbon Alloys," *Journal of Iron and Steel Institute,* **155** (1947), 321.
2 A. P. Gagnebin, K. D. Millis and N. B. Pilling, *Iron Age,* **163** (1949), Jan., 30.
3 W. C. Johnson and H. B. Smart, "The Role of Interphase Boundary Adsorption in the Formation of Spheroidal Graphite in Cast Iron," *Metallurgical Trans.,* **8A** (1977), 553.
4 S. E. Franklin and A. Stark, "Application of Secondary Ion Mass Spectrometry to Study of Graphite Morphology in Cast Iron," *Metal Science,* **18** (1984), April, 187.
5 J. Pirs and N. Mardesich, "Some Results of Investigations of the Interface Boundary Segregations in Pearlitic and Ferritic Nodular Cast Irons," *Microstructural Science,* **6** (1978), 6, 161.
6 H. Fidos, "Structural analysis of a Graphite Nodule and Surrounding Halo in Ductile Iron," *AFS International Cast Metals Journal* (1982), March, 54.
7 S. Yamamoto, B. Chang, Y. Kawano, R. Ozaki and Y. Murakami, "Producing Spheroidal Graphite Cast Iron by Suspicion of Gas Bubbles in Metals," *AFS Trans.,* **83** (1975), 217.
8 S. Yamamoto, B. Chang, Y. Kawano, R. Ozaki and Y. Murakami, "Mechanism of Nodularization of Graphite on Cast Iron Treated with Magnesium," *Metal Science,* **12** (1978), May, 239.
9 H. Itofuji, Y. Kawano, S. Yamamoto, N. Inoyama, H. Yoshida and B. Chang, "Comparison of Substructure of Compacted/Vermicular Graphite with Other Types of Graphite," *AFS Trans.,* **91** (1983), 313.
10 H. Itofuji, Y. Kawano, N. Inoyama, S. Yamamoto, B. Chang and T. Nishi, "The Formation Mechanism of Compacted/Vermicular Graphite in Cast Irons," *AFS Trans,* **91** (1983), 831.
11 B. Chang, K. Akechi and K. Hanawa, "Spheroidal Graphite Cast Iron," Agne Co. Ltd (Published 1984).
12 S. I. Karsay, "Ductile Iron Production I," Quebec Iron and Titanium Corp. (Published 1976), 13.
13 Y. Morooka, "On Spheroidal Graphite Steel; Precipitation Mechanism of Graphite," *Bulletin of the Japan Institute of Metals,* **8** (1969), 9, 598.
14 K. Kawano and T. Sawamoto, "Production of Cast Iron with Fine Granular Graphite," *AFS Trans.,* **88** (1980), 463.
15 K. Hanawa, K. Akechi, Z. Hara and T. Nakagawa, "Nodular Graphite Formation in P/M Products from Cast Iron Swarf Powder and F-Si-C Mixed Powders," *Trans. JIM,* **21** (1980), 12, 765.
16 H. Horie, T. Kowata and T. Okura, "Graphite Formation at the Bond Interface in Diffusion-bonded Spheroidal Graphite," *Imono,* **61** (1989), 7, 475.
17 Lee and Y. Kawano, "Precipitation of Spheroidal Graphite during Cooling from Liquid State in Hyper Eutectoid Steel," *Journal of the Japan Institute of Metals,* **45** (1981), 812.
18 Y. Lee and Y. Kawano, "Formation Mechanism of Precipitated Graphite Shapes in Hyper Eutectoid Steel," *Journal of the Japan Institute of Metals,* **45** (1981), 948.
19 J. Zhou, W. Schmitz and S. Engler, "Investigation of the Microstructure of Spheroidal Graphite Cast Iron for Low Solidification Rates," *Giess.-Forsch.,* **39** (1987), 2, 55.
20 A. Javaid and C. R. Loper, Jr., "Solid State Graphitization in Normalized and Annealed Ductile Cast Irons," The 94th AFS Congress, Paper No. 90-143 (1990).
21 R. Castaing, "Electron Probe Microanalysis," *Advance in Electronics and Electron Physics,* **13** (1960), 317.
22 T. Sato, M. Maruyama and T. Ototani, "Formation of Lamellar and Spheroidal Graphite in Relation to the Microsegregation of Silicon," 37th International Foundry Congress, Paper No. 5 (1970).
23 J. M. Motz and D. B. Wolters, "On Solidification Structure and Mechanical Properties in Heavy Section Ferritic SG Iron Castings, Part I, Microsegregations," *Giess.-Forsch.,* **40** (1988), 2, 69.
24 K. S. Lee and M. Kayama, *Imono* (1976), Oct. 30, 11.
25 M. C. Speer and N. A. D. Parlee, "Dissolution and Desulfurization Reactions of Magnesium Vapour in Liquid Iron Alloys," *AFS Cast Metals Research Journal* (1972), Sept., 122.